

Giant anomalous Hall angle in a half-metallic magnetic Weyl semimetal

Enke Liu^{1,2*}, Yan Sun^{1*}, Lukas Mchler³, Aili Sun¹, Lin Jiao¹, Johannes Kroder¹, Vicky S¹,
Horst Borrmann¹, Wenhong Wang², Walter Schnelle¹, Steffen Wirth¹, Sebastian T. B.
Goennenwein⁴, and Claudia Felser¹

¹ *Max-Planck Institute for Chemical Physics of Solids, 01187 Dresden, Germany*

² *Institute of Physics, Chinese Academy of Sciences, Beijing 100190, China*

³ *Department of Chemistry, Princeton University, Princeton, New Jersey 08544, USA*

⁴ *Institut fr Festkrper- und Materialphysik, Technische Universitt Dresden, 01062 Dresden, Germany*

(Dated: 22 November 2017)

Magnetic Weyl semimetals (WSMs) with time reversal symmetry breaking exhibit Weyl nodes that act as monopoles of Berry curvature and are thus expected to generate a large intrinsic anomalous Hall effect (AHE). However, in most magnetic WSMs, the Weyl nodes are located far from the Fermi energy, making it difficult to observe the Weyl-node dominated intrinsic AHE in experiments. Here we report a novel half-metallic magnetic WSM in the Kagomlattice Shandite compound $\text{Co}_3\text{Sn}_2\text{S}_2$. The Weyl nodes, linked by gapped nodal rings, are crucially located just 60 meV above the Fermi energy. Owing to both the significantly enhanced Berry curvature arising from the Weyl bands and the low charge conductivity, the anomalous Hall conductivity (AHC) and anomalous Hall angle (AHA) experimentally reach up to $1130 \Omega^{-1} \text{cm}^{-1}$ and 20% respectively, which allows the material to simultaneously host a large AHC and giant AHA. Interpreting WSMs as coupled quantum AHE layers, the present results suggest that thin films of this quasi-two-dimensional WSM present a promising candidate for the bulk-insulating quantum AHE. $\text{Co}_3\text{Sn}_2\text{S}_2$ as an easy-to-grow magnetic WSM thus represents an ideal platform to study Weyl physics. Our findings further suggest half-metallic Weyl semimetals – combining a topological Weyl phase for one spin channel with a band gap for the other – as a new paradigm for materials with a large Berry-in-origin AHE.

* Enke.Liu@cpfs.mpg.de (E. L.)

* Yan.Sun@cpfs.mpg.de (Y. S.)

As an important electronic transport phenomenon, the anomalous Hall effect (AHE) is typically attributed to two different originating mechanisms, namely, extrinsic contributions arising from scattering effects, and intrinsic contributions arising from the Berry curvature¹⁻⁵. In particular, such Berry curvature arises from the entangled Bloch electronic bands with spin-orbital coupling (SOC) when spatial inversion or time reversal symmetry (TRS) of the system is broken^{6,7}. A quantum anomalous Hall insulator can be considered as the two-dimensional limit of the three-dimensional AHE systems^{8,9}. In these materials, the anomalous Hall conductivity (AHC) is quantized due to the presence of a bulk gap and dissipationless edge states¹⁰⁻¹³. Interestingly, a Weyl semimetal (WSM) with broken TRS can be interpreted as a stacked heterostructure of such quantum anomalous Hall insulator layers^{14,15}. The coupling between the layers closes the bulk band gap at isolated points in the Brillouin zone (BZ) where the Weyl nodes are located. While the AHC in a bulk WSM is not quantized, there is still a universal contribution from the Weyl nodes due to the unique Berry curvature distribution in these materials^{3,4,16}. Moreover, since the Weyl points are topologically protected, the large contribution to the AHE arising from the Weyl points does not require a high charge carrier density^{3,17}. In fact, the density of state in ideal WSMs vanishes at the Weyl nodes where the AHC is at a maximum^{1,4}. As a result, magnetic WSMs are expected to exhibit a large anomalous Hall angle (AHA), which could lead to the developments of spintronic devices with reduced energy costs.

A number of promising candidates for such TRS-broken magnetic WSM materials have already been proposed, including $\text{Y}_2\text{Ir}_2\text{O}_7$ (18), HgCr_2Se_4 (19), and certain Co_2 -based Heusler compounds²⁰⁻²². Indeed, an AHA of ~16% was recently observed at low temperatures in the magnetic-field induced WSM GdPtBi (23). However, neither a large AHC nor a large AHA has yet been reported in magnetic WSMs with intrinsically broken TRS in the absence of a magnetic field. One possible reason for this is that the Weyl nodes in most magnetic WSMs are located far from the Fermi level, and the corresponding electron transport contribution is thus negligible. The search for intrinsic magnetic WSMs with Weyl nodes close to the Fermi level is therefore not only an efficient strategy to obtain materials exhibiting both a high AHE

and large AHA, but also important for a comprehensive understanding of the Weyl topological effects on the AHE in real materials.

The Shandite phase of $\text{Co}_3\text{Sn}_2\text{S}_2$ is known to be a ferromagnet with a Curie temperature (T_C) = 177 K and a magnetic moment = $0.29 \mu_B/\text{Co}$ (24-26). Magnetization measurements confirmed that the easy axis of the magnetization lies along the c -axis²⁷, while photoemission and band structure calculations revealed that below T_C , $\text{Co}_3\text{Sn}_2\text{S}_2$ exhibits Type IA half-metallic ferromagnetic order whose spin-minority states are gapped^{28,29}. In this work, we demonstrate that $\text{Co}_3\text{Sn}_2\text{S}_2$ is a magnetic WSM with six pairs of Weyl points located just 60 meV above the Fermi level. On account of its topologically non-trivial electronic structure, $\text{Co}_3\text{Sn}_2\text{S}_2$ exhibits a large intrinsic AHC arising from the Berry curvature distribution, which is dominated by the SOC-gapped nodal lines around the Weyl nodes. Accompanying the large AHC and the small carrier density, (i.e., low charge conductivity), an AHA as large as 20% is observed in the temperature range of 100 – 150 K. Thus, $\text{Co}_3\text{Sn}_2\text{S}_2$ and similar half-metallic WSMs not only emerge as ideal materials for achieving both large AHC and AHA, but also provide a promising material for the comprehensive study of the physics of magnetic Weyl fermions without the need of an external magnetic field.

Figure 1 summarizes the structural and electronic properties of $\text{Co}_3\text{Sn}_2\text{S}_2$. As shown in Fig. 1a, $\text{Co}_3\text{Sn}_2\text{S}_2$ crystallizes in a rhombohedral structure of the space group, $R\bar{3}m$ (no. 166)(24). The crystal is seen to possess a quasi-2D Co_3Sn layer sandwiched between S atoms, with the magnetic Co atoms arranged on a Kagomé lattice in the a - b plane in the hexagonal representation of the space group. Owing to magnetic anisotropy, the magnetic moments are oriented along the c -axis, and the magnetism is quasi-2D in nature²⁷. By itself, this dimensional restriction of the magnetization may be responsible for some of the interesting electronic and magnetic properties of this compound. In the following, we performed band structure calculations of $\text{Co}_3\text{Sn}_2\text{S}_2$ with the spin polarization along the c -axis. The calculated magnetic moments without and with SOC are 0.33 and $0.30 \mu_B/\text{Co}$, respectively, which are very close to the experimental values of $0.29 \mu_B/\text{Co}$ obtained from neutron diffraction²⁶, $0.31 \mu_B/\text{Co}$ from magnetization measurement²⁷, and confirmed by our measured result ($0.30 \mu_B/\text{Co}$)

(see [Supplementary Information](#)). As expected, the calculation including SOC gives a more accurate result.

The band structures of $\text{Co}_3\text{Sn}_2\text{S}_2$ calculated without and with SOC are shown in Fig. 1b. The bands corresponding to the spin-down channel are insulating in character with a gap of 0.35 eV, while the spin-up channel crosses the Fermi level and thus has a metallic character. This half-metallic behaviour is consistent with the results of previous reports on this compound²⁷⁻²⁹. Furthermore, for the spin-up states, we observe linear band crossings along the Γ -L and L-U paths, just slightly above and below the Fermi energy, respectively. For finite SOC, these linear crossings open small gaps with band anti-crossings, and make this compound semimetal-like. When these results are considered in connection with the ferromagnetism of $\text{Co}_3\text{Sn}_2\text{S}_2$ (24-27), they suggest that a TRS-breaking WSM phase might be hidden in this compound.

In order to confirm this prediction, the single crystals of $\text{Co}_3\text{Sn}_2\text{S}_2$ were grown for further experimental investigations (see Methods and [Supplementary Information](#)). The basic information is shown here. The high quality of the single crystals was confirmed by X-ray diffraction (XRD) pattern showing clear and sharp spots (see Fig. 1c) as well as from structure refinement for a small single crystal chipped off the large crystal. Further confirmation comes from scanning tunneling microscopy (STM) showing topographic image of the hexagonal array of the (0001) crystal surface (see Fig. 1d). Magnetization measurements confirmed a Curie temperature of $T_C = 175$ K and a saturation magnetization = $0.30 \mu_B/\text{Co}$ (see [Supplementary Information](#)). As could be expected from our band structure calculations (Fig. 1b), further evidence of a semimetal-like behaviour is observed in temperature dependent longitudinal charge resistivity ρ , which shows a moderate residual resistivity of $\sim 50 \mu\Omega \text{ cm}$, i.e., a moderate charge conductivity $\sigma \sim 2 \times 10^4 \Omega^{-1} \text{ cm}^{-1}$ at 2 K (Fig. 1e).

In order to analyze the topological character of $\text{Co}_3\text{Sn}_2\text{S}_2$ suggested by Fig. 1b, we now consider the linear band crossings in more detail. The space group $R\bar{3}m$ of $\text{Co}_3\text{Sn}_2\text{S}_2$ has one mirror plane M_{010} . Without SOC, the interaction between spin-up and spin-down states is

ignored and the mirror plane is a high symmetry plane of the Hamiltonian. Thus, as they are protected by this mirror symmetry, the linear band crossing identified in Fig. 1b form a nodal ring in the mirror plane based on the band inversion, as shown in Fig. 2a. Moreover, the linear crossings between the L- Γ and L-U paths are just single points on the ring. When the C_{3z} -rotation and inversion symmetries of the material are considered, one finds a total of six nodal rings in the BZ, as shown schematically in Fig. 2b.

Upon taking SOC into account, the spin s_z is no longer a good quantum number and the mirror symmetry of the Hamiltonian is broken, which causes the linear crossings of the nodal lines to split, as presented in Fig. 2c. Interestingly, one pair of linear crossing points remains in the form of Weyl nodes along the former nodal line. These two Weyl nodes act as a monopole sink and source of Berry curvature (see [Supplementary Information](#)) and possess opposite topological charges of +1 and -1, respectively. In total, there are three such pairs of Weyl nodes in the first BZ due to the inversion and C_{3z} -rotation symmetries of the crystal, and their distribution is presented in Fig. 2b. It is important to emphasize that the Weyl nodes in $\text{Co}_3\text{Sn}_2\text{S}_2$ are only 60 meV above the charge neutrality point, which is much closer to the Fermi energy than previously proposed magnetic WSMs. These Weyl nodes and non-trivial Weyl nodal rings together make this material exhibit a clean topological band structure around the E_F . As a result, the Weyl node-dominated physics in $\text{Co}_3\text{Sn}_2\text{S}_2$ should be prominent and easy to detect in experiments.

We now address the AHE response of $\text{Co}_3\text{Sn}_2\text{S}_2$ that can be expected from the particular band structure properties outlined above. In order to obtain a complete topological character, we integrated the Berry curvature $\Omega_{yx}^z(k)$ along k_z in the BZ. Our results reveal two main types of hot spots for the integrated Berry curvature: One that is located around the Weyl nodes, and the other near the edge of the nodal lines (see Fig. 2d). To investigate the origin of the hot spot of the Berry curvature distribution, we choose the $k_y = 0$ plane, which includes two nodal rings and two pairs of Weyl nodes, as shown in Fig. 2e. We note that hot spots of the integrated Berry curvature are primarily determined by the shape of the nodal lines, and both types of hot spots observed here originate from the nodal-line-like band anti-crossing

behaviour. Along the nodal ring, the component of the Berry curvature parallel to k_z leads to the larger hot spot we observe, while a different part around the Weyl node contributes to the smaller hot spot. Owing to the half-metallic band anti-crossing behaviour and the position of the six Weyl nodal rings around the Fermi level, the calculated Berry curvature is clean and large, which should yield fascinating spin-electronic transport behaviours including a large intrinsic AHE³. The energy dependent AHC calculated from the Berry curvature is shown in Fig. 2f. As one can see from the figure, a large peak in σ_{yx} appears around E_F with a maximum of $1100 \Omega^{-1} \text{cm}^{-1}$. Since the AHC depends on the location of the Fermi level (see Eq. (1), Methods), it usually changes sharply as a function of energy. However, the peak in σ_{yx} in Fig. 2f stays above $1000 \Omega^{-1} \text{cm}^{-1}$ within an energy window of 100 meV below E_F . Therefore, we expect to observe a high AHC in experiments for charge neutral or slightly *p*-doped $\text{Co}_3\text{Sn}_2\text{S}_2$ samples.

The strong AHE induced by the band structure topology is indeed directly verified by our transport measurements, which were performed on an out-of-plane configuration of $I // x$ [$2\bar{1}\bar{1}0$] and $B // z$ [0001] (see Fig. 1e). As we observe in Fig. 3a, the anomalous Hall conductivity (σ_H^A), calculated from $\sigma_H^A = -\rho_H^A / ((\rho_H^A)^2 + \rho^2)$ (ρ_H^A is anomalous Hall resistivity and derived by extrapolating the high-field part of ρ_H back to zero field (see [Supplementary Information](#)); ρ is the longitudinal charge resistivity at zero field), shows a maximum of $1130 \Omega^{-1} \text{cm}^{-1}$ at 2 K, which is in very good agreement with our predicted theoretical value (σ_{yx} , Fig. 2f). We also studied the in-plane case ($I // x$ [$2\bar{1}\bar{1}0$] and $B // y$ [$01\bar{1}0$]), for which the AHC disappears (not shown), due to strong magnetic and Berry-curvature anisotropies. Moreover, at temperatures below 100 K ($T < T_C$), for the out-of-plane case $\sigma_H^A \sim 1000 \Omega^{-1} \text{cm}^{-1}$ is revealed to be independent of temperature (see also the inset of Fig. 3a, and note the logarithmic vertical axis). This robust behaviour against temperature indicates that the AHE is not governed by scattering events in the system. In addition, σ_H shows rectangular hysteresis loops with very sharp switching (Fig. 3b), and the coercive field is seen to increase with decreasing temperature, resulting in a value of 0.33 T at 2 K (also see [Supplementary](#)

Information). As is evident from the figure, a large remanent Hall effect at zero field is observed in this material.

We plot ρ_H^A as a function of temperature in Fig. 3c. A large peak in ρ_H^A with a maximum of 44 $\mu\Omega$ cm appears at 150 K. When σ_H^A is plotted against σ , as presented in Fig. 3d, we also find that σ_H^A is nearly independent of σ (i.e., $\sigma_H^A \sim (\sigma)^0 = \text{constant}$) for temperatures below 100 K, as is expected for an intrinsic AHE in the framework of the unified model for AHE physics (see [Supplementary Information](#) for more details)^{30,31}. This independence of ρ_H^A with respect to both T and ρ indicates that the AHE only originates from the intrinsic scattering-independent mechanism, and is thus dominated by the Berry curvature in momentum space². This present scaling behaviour is well consistent with our first-principles calculations.

In addition to a large AHC, and arguably more importantly, $\text{Co}_3\text{Sn}_2\text{S}_2$ also features a giant AHA that can be characterized by the ratio of σ_H^A/σ . The temperature dependence of the AHA is shown in Fig. 4a. With increasing temperature, the AHA first increases from 5.6% at 2 K, reaching a maximum of $\sim 20\%$ around 120 K, before decreasing again as the temperature increases above T_C . The contour plot of σ_H/σ with respect to B and T is depicted in Fig. 4b, and makes it intuitively clear that a giant Hall angle appears between 75 – 175 K irrespective of the magnetic field magnitude. This can be straightforwardly understood by considering that the AHC in $\text{Co}_3\text{Sn}_2\text{S}_2$ arises from the Berry curvature of the occupied states. The band topology of these states is basically unaffected by the small energy scale of thermal excitations up to room temperature³². In other words, the topologically protected AHC (σ_H^A) is relatively robust against temperature. In contrast, the Weyl-node-related charge conductivity (σ) is sensitive to temperature due to electron–phonon scattering³³. These behaviours are shown clearly in Fig. 3a. Therefore, the AHA is expected to increase with increasing temperature in a wide temperature range below T_C . From Fig. 3a and the ρ_H - B data (see [Supplementary Information](#)), one can extract values for the relatively low charge conductivity ($\sigma \sim 2 \times 10^4 \Omega^{-1} \text{cm}^{-1}$ at 2 K and $0.5 \times 10^4 \Omega^{-1} \text{cm}^{-1}$ at 120 K) and the relatively small carrier density ($n \sim 10^{21} \text{cm}^{-3}$), which support our characterizations of the typical

semi-metallic features of this WSM. This semi-metallicity largely improves the value of σ_H^A/σ in this material.

When compared to previously reported results for other AHE materials (see Fig. 4c), the value of AHA in $\text{Co}_3\text{Sn}_2\text{S}_2$ observed in this work is seen to be the largest by quite a prominent margin. For most of these materials — formed mainly of ferromagnetic transition metals and alloys — the AHCs originate from topologically trivial electronic bands. A typical feature of these materials is that both the AHC and the charge conductivity are either large or small and therefore the AHA of these materials typically cannot be large. While the magnetic-field-induced Weyl semimetal GdPtBi has a large AHA of 16%, its AHC is very small, and moreover, it requires an external field to induce the Weyl phase²³. In contrast, owing to Weyl effects and its semi-metallic character, $\text{Co}_3\text{Sn}_2\text{S}_2$ possesses both a large AHC and giant AHA simultaneously and at zero magnetic field, which promotes this system to quite a different position among the known AHE materials. As a consequence, a large anomalous Hall current can be expected in thin films of this material that may even reach the limit of a quantized AHE with dissipationless quantum Hall edge states^{13,34-36}. In more general terms, a clean topological band structure induces both a large AHC and giant AHA (as demonstrated here for the half-metallic WSM $\text{Co}_3\text{Sn}_2\text{S}_2$), and so can be seen as a guide for the realization of strong AHE in magnetic half-metallic topological semimetals.

In summary, a WSM phase arises in the TRS-breaking ferromagnetic half-metallic compound $\text{Co}_3\text{Sn}_2\text{S}_2$ below T_C . As they are protected by the topological electronic structure, significantly enhanced Berry curvature is generated along the gap-opening path due to SOC, resulting in a high AHC of over $1100 \text{ } \Omega^{-1} \text{ cm}^{-1}$. Owing to the semi-metallic band structure and the resulting low charge carrier density, $\text{Co}_3\text{Sn}_2\text{S}_2$ further possesses an AHA as large as 20% across a wide temperature range. $\text{Co}_3\text{Sn}_2\text{S}_2$ thus represents the first material hosting both a large AHC and a giant AHA, and forms an important progress in the study of AHE physics connected to intrinsic band Berry-phase curvature. This Kagomé-lattice magnetic WSM also promises to be an ideal candidate for developing a quantum anomalous Hall insulator due to its quasi-2D ferromagnetism without doping and clean electronic structure around the Fermi

energy^{9,13,34,35}. Moreover, it is easy to grow large high-quality single crystals, which makes $\text{Co}_3\text{Sn}_2\text{S}_2$ and similar half-metal systems excellent platforms for comprehensive studies of magnetic Weyl physics³⁷⁻⁴⁰ and related topological phase transitions^{41,42}, as well as for the realization of future spintronic devices with reduced energy costs^{43,44}. Our findings further suggest that, in general, a strong AHE originating from Berry curvature can be observed in a broad class of TRS-breaking half-metallic Weyl semimetals with gapped nodal lines close to the Fermi energy.

Methods

$\text{Co}_3\text{Sn}_2\text{S}_2$ single crystals. We grew the single crystals by different methods. The crystals were characterized by powder X-ray diffraction as single phase with a Shandite-type structure. The lattice parameters at room temperature are $a = 5.3689 \text{ \AA}$ and $c = 13.176 \text{ \AA}$. The single crystals and orientations were confirmed by single-crystal X-ray diffraction technique. Topographic images of the crystal surface were characterized by a cryogenic scanning tunneling microscopy (STM), taken at conditions of $T = 2.5 \text{ K}$, a bias voltage of $V_b = 100 \text{ mV}$, and a tunnel current of $I_t = 500 \text{ pA}$. The sample was cleaved *in situ* ($p \leq 2 \times 10^{-9} \text{ Pa}$) at about 20 K .

Magnetization and transport measurements. Magnetization measurements were carried out on oriented crystals with the magnetic field applied along both the a and c axes using a vibrating sample magnetometer (MPMS 3, Quantum Design). The transport measurements were performed on a PPMS 9 (Quantum Design) using the low-frequency alternating current (ACT) option. The four-probe method was used to measure the longitudinal charge resistivity, while for the Hall resistivity measurements, the five-probe method was used with a balance protection meter to eliminate possible magnetoresistance signals. The charge and Hall resistivities were measured alternatively at each temperature. The transport measurements presented in this work were performed on an out-of-plane configuration of $I // x$ $[\bar{2}1\bar{1}0]$ and $B // z$ $[0001]$ with rectangular axis and on a rectangular sample with dimensions of $0.8 \times 0.36 \times 3.8 \text{ mm}^3$.

DFT calculations. The electronic structure calculations were performed based on the density functional theory using the Vienna *ab-initio* simulation package (VASP)⁴⁵. The exchange and correlation energies were considered in the gradient approximation (GGA), following the Perdew–Burke–Ernzerhof parametrization scheme⁴⁶. When calculating the AHC and Berry curvature, we projected the Bloch wave functions into Wannier functions⁴⁷. Based on the corresponding Hamiltonian constructed from Wannier orbitals, the AHC was calculated by the Kubo formula approach in the linear response and clean limit⁴:

$$\sigma_{yx}^z(E_F) = e^2 \hbar \left(\frac{1}{2\pi} \right)^3 \int_{\vec{k}} d\vec{k} \sum_{E(n,\vec{k}) < E_F} f(n,\vec{k}) \Omega_{n,yx}^z(\vec{k})$$

$$\Omega_{n,yx}^z(\vec{k}) = \text{Im} \sum_{n' \neq n} \frac{\langle u(n,\vec{k}) | \hat{v}_y | u(n',\vec{k}) \rangle \langle u(n',\vec{k}) | \hat{v}_x | u(n,\vec{k}) \rangle - (x \leftrightarrow y)}{(E(n,\vec{k}) - E(n',\vec{k}))^2} \quad (1)$$

where $f(n,\vec{k})$ is the Fermi-Dirac distribution, $E(n,\vec{k})$ is the eigen-value of the n -th eigen-state of $|u(n,\vec{k})\rangle$ at \vec{k} point, and $\hat{v}_{x(y)} = \frac{1}{\hbar} \frac{\partial H(\vec{k})}{\partial k_{x(y)}}$ is the velocity operator. The numerical integration was performed using a $501 \times 501 \times 501$ k -grid.

References

1. Fang, Z. *et al*. The anomalous Hall effect and magnetic monopoles in momentum space. *Science* **302**, 92-95 (2003).
2. Nagaosa, N., Sinova, J., Onoda, S., MacDonald, A. H. and Ong, N. P. Anomalous Hall effect. *Rev. Mod. Phys.* **82**, 1539-1592 (2010).
3. Haldane, F. D. M. Berry curvature on the Fermi surface: Anomalous Hall effect as a topological Fermi-liquid property. *Phys. Rev. Lett.* **93**, 206602 (2004).
4. Xiao, D., Chang, M. C. and Niu, Q. Berry phase effects on electronic properties. *Rev. Mod. Phys.* **82**, 1959-2007 (2010).
5. Nakatsuji, S., Kiyohara, N. and Higo, T. Large anomalous Hall effect in a non-collinear antiferromagnet at room temperature. *Nature* **527**, 212-215 (2015).
6. Weng, H. M., Fang, C., Fang, Z., Bernevig, B. A. and Dai, X. Weyl semimetal phase in noncentrosymmetric transition-metal monophosphides. *Phys. Rev. X* **5**, 011029 (2015).
7. Yan, B. and Felser, C. Topological materials: Weyl semimetals. *Annu. Rev. Condens. Matter Phys.* **8**, 337-354 (2017).
8. Weng, H. M., Yu, R., Hu, X., Dai, X. and Fang, Z. Quantum anomalous Hall effect and related topological electronic states. *Adv. Phys.* **64**, 227-282 (2015).
9. Liu, C.-X., Zhang, S.-C. and Qi, X.-L. The quantum anomalous Hall effect: Theory and experiment. *Annu. Rev. Condens. Matter Phys.* **7**, 301-321 (2016).
10. Yu, R. *et al*. Quantized anomalous Hall effect in magnetic topological insulators. *Science* **329**, 61-64 (2010).
11. Chang, C.-Z. *et al*. Experimental observation of the quantum anomalous Hall effect in a magnetic topological insulator. *Science* **340**, 167-170 (2013).
12. Fang, C., Gilbert, M. J. and Bernevig, B. A. Large-Chern-number quantum anomalous Hall effect in thin-film topological crystalline insulators. *Phys. Rev. Lett.* **112**, 046801 (2014).
13. Kou, X. *et al*. Scale-invariant quantum anomalous Hall effect in magnetic topological insulators beyond the two-dimensional limit. *Phys. Rev. Lett.* **113**, 137201 (2014).

14. Burkov, A. A. and Balents, L. Weyl semimetal in a topological insulator multilayer. *Phys. Rev. Lett.* **107**, 127205 (2011).
15. Zyuzin, A. A., Wu, S. and Burkov, A. A. Weyl semimetal with broken time reversal and inversion symmetries. *Phys. Rev. B* **85**, 165110 (2012).
16. Burkov, A. A. Anomalous Hall effect in Weyl metals. *Phys. Rev. Lett.* **113**, 187202 (2014).
17. Wang, X., Vanderbilt, D., Yates, J. R. and Souza, I. Fermi-surface calculation of the anomalous Hall conductivity. *Phys. Rev. B* **76**, 195109 (2007).
18. Wan, X. G., Turner, A. M., Vishwanath, A. and Savrasov, S. Y. Topological semimetal and Fermi-arc surface states in the electronic structure of pyrochlore iridates. *Phys. Rev. B* **83**, 205101 (2011).
19. Xu, G., Weng, H. M., Wang, Z. J., Dai, X. and Fang, Z. Chern semimetal and the quantized anomalous Hall effect in HgCr_2Se_4 . *Phys. Rev. Lett.* **107**, 186806 (2011).
20. K  bler, J. and Felser, C. Weyl points in the ferromagnetic Heusler compound Co_2MnAl . *EPL* **114**, 47005 (2016).
21. Wang, Z. J. *et al.* Time-reversal-breaking Weyl fermions in magnetic Heusler alloys. *Phys. Rev. Lett.* **117**, 236401 (2016).
22. Chang, G. Q. *et al.* Room-temperature magnetic topological Weyl fermion and nodal line semimetal states in half-metallic Heusler Co_2TiX ($\text{X}=\text{Si}$, Ge , or Sn). *Sci. Rep.* **6**, 38839 (2016).
23. Suzuki, T. *et al.* Large anomalous Hall effect in a half-Heusler antiferromagnet. *Nat. Phys.* **12**, 1119-1123 (2016).
24. Weihrich, R., Anusca, I. and Zabel, M. Half-antiperovskites: Structure and type-antitype relations of Shandites $\text{M}_{3/2}\text{AS}$ ($\text{M} = \text{Co}, \text{Ni}$; $\text{A} = \text{In}, \text{Sn}$). *Z. Anorg. Allg. Chem.* **631**, 1463-1470 (2005).
25. Weihrich, R. and Anusca, I. Half antiperovskites. III - Crystallographic and electronic structure effects in $\text{Sn}_{2-x}\text{In}_x\text{Co}_3\text{S}_2$. *Z. Anorg. Allg. Chem.* **632**, 1531-1537 (2006).
26. Vaqueiro, P. and Sobany, G. G. A powder neutron diffraction study of the metallic ferromagnet $\text{Co}_3\text{Sn}_2\text{S}_2$. *Solid State Sci.* **11**, 513-518 (2009).

27. Schnelle, W. *et al.* Ferromagnetic ordering and half-metallic state of $\text{Sn}_2\text{Co}_3\text{S}_2$ with the Shandite-type structure. *Phys. Rev. B* **88**, 144404 (2013).
28. Dedkov, Y. S., Holder, M., Molodtsov, S. L. and Rosner, H. Electronic structure of shandite $\text{Co}_3\text{Sn}_2\text{S}_2$. *J. Phys. Conf. Ser.* **100** (2008).
29. Holder, M. *et al.* Photoemission study of electronic structure of the half-metallic ferromagnet $\text{Co}_3\text{Sn}_2\text{S}_2$. *Phys. Rev. B* **79** (2009).
30. Onoda, S., Sugimoto, N. and Nagaosa, N. Intrinsic versus extrinsic anomalous Hall effect in ferromagnets. *Phys. Rev. Lett.* **97**, 126602 (2006).
31. Miyasato, T. *et al.* Crossover behavior of the anomalous Hall effect and anomalous Nernst effect in itinerant ferromagnets. *Phys. Rev. Lett.* **99**, 086602 (2007).
32. Yue, D. and Jin, X. Towards a better understanding of the anomalous Hall effect. *J. Phys. Soc. Jpn.* **86**, 011006 (2016).
33. Gantmakher, V. F. The experimental study of electron-phonon scattering in metals. *Rep. Prog. Phys.* **37**, 317 (1974).
34. Ohgushi, K., Murakami, S. and Nagaosa, N. Spin anisotropy and quantum Hall effect in the kagome lattice: Chiral spin state based on a ferromagnet. *Phys. Rev. B* **62**, R6065-R6068 (2000).
35. Checkelsky, J. G. *et al.* Trajectory of the anomalous Hall effect towards the quantized state in a ferromagnetic topological insulator. *Nat. Phys.* **10**, 731-736 (2014).
36. Samarth, N. Quantum materials discovery from a synthesis perspective. *Nat. Mater.* **16**, 1068-1076 (2017).
37. Kuroda, K. *et al.* Evidence for magnetic Weyl fermions in a correlated metal. *Nat. Mater.* **16**, 1090-1095 (2017).
38. Chan, C.-K., Lee, P. A., Burch, K. S., Han, J. H. and Ran, Y. When chiral photons meet chiral Fermions: Photoinduced anomalous Hall effects in Weyl semimetals. *Phys. Rev. Lett.* **116**, 026805 (2016).
39. Ikhlas, M. *et al.* Large anomalous Nernst effect at room temperature in a chiral antiferromagnet. *Nat. Phys.* **13**, 1085-1090 (2017).

40. Rajamathi, C. R. *et al*. Weyl semimetals as hydrogen evolution catalysts. *Adv. Mater.* **29**, DOI: 10.1002/adma.201606202 (2017).
41. Yang, B.-J., Moon, E.-G., Isobe, H. and Nagaosa, N. Quantum criticality of topological phase transitions in three-dimensional interacting electronic systems. *Nat. Phys.* **10**, 774 (2014).
42. Ahn, J. and Yang, B.-J. Unconventional topological phase transition in two-dimensional systems with space-time inversion symmetry. *Phys. Rev. Lett.* **118**, 156401 (2017).
43. Kurebayashi, D. and Nomura, K. Voltage-driven magnetization switching and spin pumping in Weyl semimetals. *Phys. Rev. Appl.* **6**, 044013 (2016).
44. Tokura, Y., Kawasaki, M. and Nagaosa, N. Emergent functions of quantum materials. *Nat. Phys.* **13**, 1056-1068 (2017).
45. Kresse, G. and Furthmüller, J. Efficient iterative schemes for *ab initio* total-energy calculations using a plane-wave basis set. *Phys. Rev. B* **54**, 11169-11186 (1996).
46. Perdew, J. P., Burke, K. and Ernzerhof, M. Generalized gradient approximation made simple. *Phys. Rev. Lett.* **77**, 3865-3868 (1996).
47. Mostofi, A. A. *et al*. wannier90: A tool for obtaining maximally-localised Wannier functions. *Comput. Phys. Commun.* **178**, 685-699 (2008).

Acknowledgements

This work was financially supported by the European Research Council (ERC) Advanced Grant (No. 291472) 'IDEA Heusler!' and ERC Advanced Grant (No. 742068) 'TOPMAT'. E.L. acknowledges supports from Alexander von Humboldt foundation of Germany for his Fellowship and from National Natural Science Foundation of China for his Excellent Young Scholarship (No. 51722106). E. L. and W. W. thank the National Key R&D Program of China (No. 2017YFA0206303).

Author contributions

The project was conceived by E.L. and C.F. E.L. grew the single crystals and performed the structural, magnetic and transport measurements with the assistances from A.S., J.K., V.S., H.B. and W.S. The STM characterizations were performed by L.J. and S.W. The theoretical calculations were carried out by Y.S., L.M. and E.L. The paper was written by E.L., Y.S. and S.T.B.G. with important inputs from L.M., W.S., S.W. and W.W. All authors discussed the results and commented on the manuscript. The project was supervised by C.F.

Competing financial interests

The authors declare no competing financial interests.

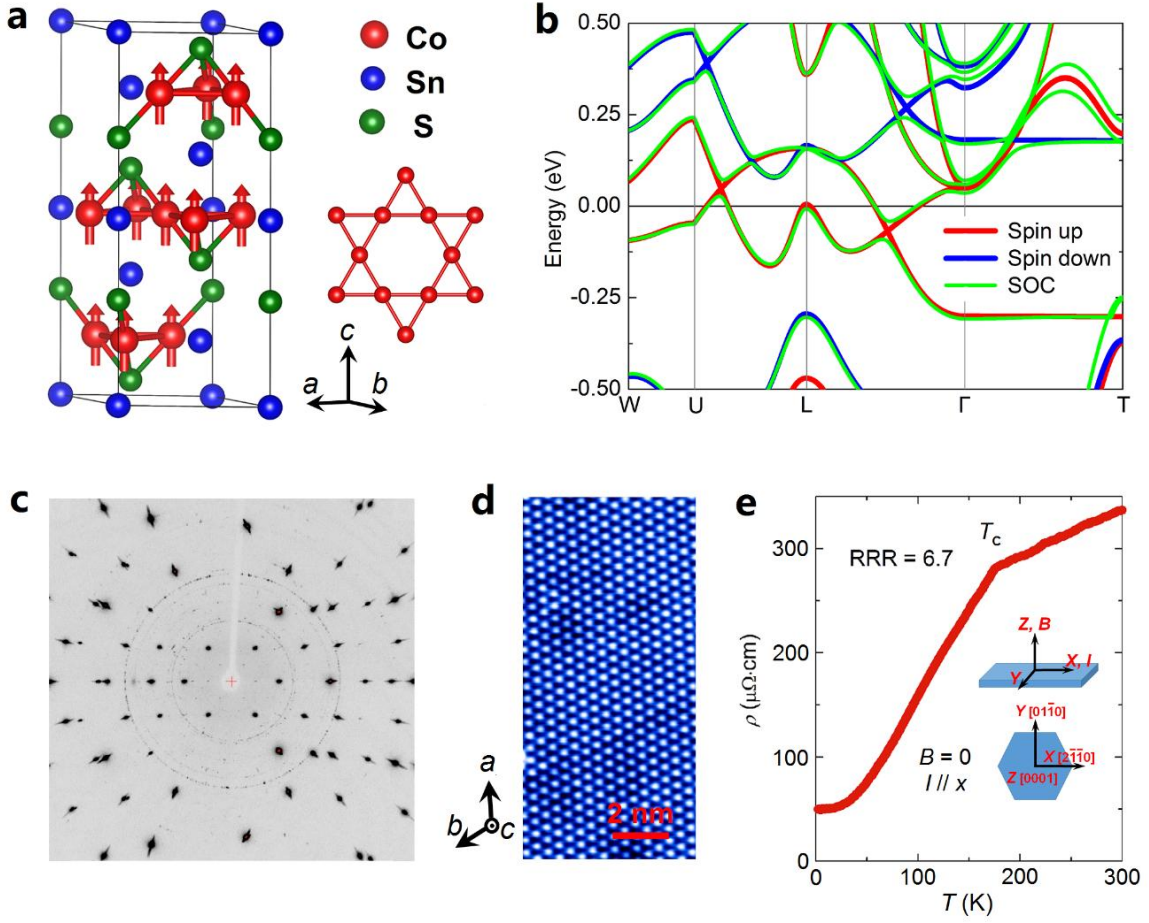


Figure 1 | Crystal and electronic structures of $\text{Co}_3\text{Sn}_2\text{S}_2$ and the measured electrical resistivity. **a**, Unit cell in hexagonal setting. The Co atoms form a quasi-2D Kagomé lattice whose magnetic moments align along the c -axis. **b**, Energy dispersion of electronic bands along high-symmetry paths without and with SOC, respectively. The labels of high-symmetry points are given in Fig. 2b. **c**, Single-crystal XRD pattern after rocking by 32° about a -axis of the rhombohedral cell. Sharp and distinct diffraction spots prove the high quality of the crystal. The faint powder rings may be assigned to distortions and contaminations on the surface. **d**, STM real-space topographic image of the (0001) surface showing a hexagonal array, obtained after *in situ* low-temperature cleaving. **e**, Temperature dependence of the longitudinal charge resistivity ρ , with a RRR (i.e., $\rho_{300\text{K}}/\rho_{2\text{K}}$) value of 6.7 and a residual resistivity of $\rho_{2\text{K}} \sim 50 \mu\Omega \text{ cm}$, i.e., a charge conductivity of $\sigma \sim 2 \times 10^4 \Omega^{-1} \text{ cm}^{-1}$ at 2 K. All transport measurements shown in this study were performed on an out-of-plane configuration of $I \parallel x$ [$2\bar{1}\bar{1}0$] and $B \parallel z$ [0001] with rectangular axis. Here x and z axes are respectively parallel to a and c ones shown in **a**.

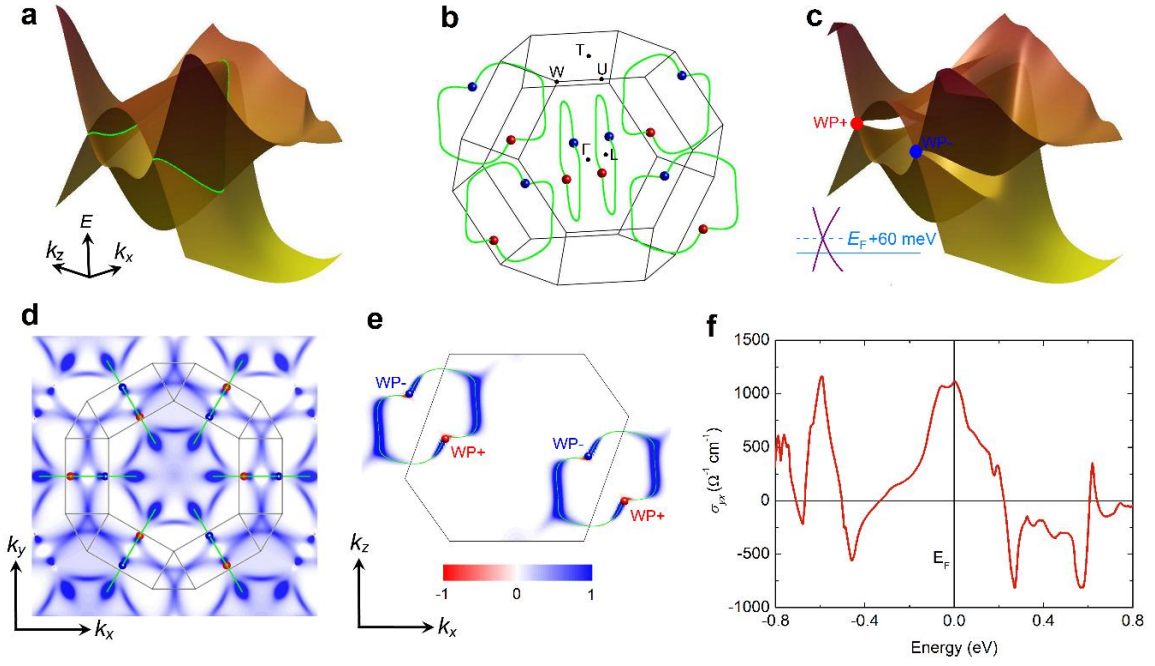


Figure 2 | Theoretical calculations of the Berry curvature and AHC. **a**, Linear band crossings form a nodal ring in the mirror plane. **b**, Side and top views of the nodal rings and distribution of the Weyl points in the BZ. **c**, SOC breaks the nodal ring band structure into opened gaps and Weyl nodes. The Weyl nodes are located just 60 meV above the Fermi level, and the gapped nodal lines are distributed around the Fermi level. **d**, Berry curvature distribution projected to the k_x - k_y plane. **e**, Berry curvature distribution in the $k_y = 0$ plane. The color bar for **d** and **e** are in arbitrary units. **f**, Energy dependence of the AHC in terms of the components of $\Omega_{yx}^z(k)$.

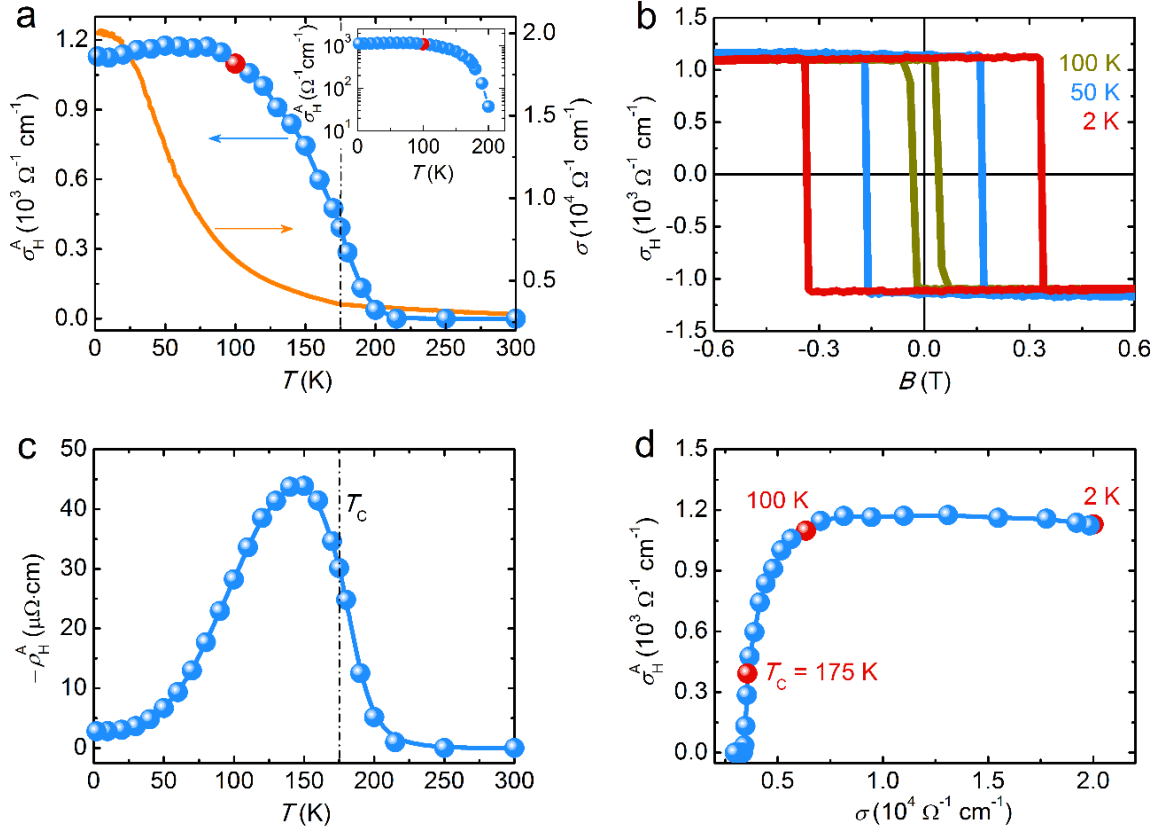


Figure 3 | Transport measurements of the AHE. **a**, Temperature dependence of the AHC (σ_H^A) and the longitudinal conductivity σ at zero magnetic field. The inset shows the logarithmic temperature dependence of σ_H^A . **b**, Field dependence of the Hall conductivity σ_H at 100, 50, and 2 K with $I \parallel x$ $[2\bar{1}10]$ and $B \parallel z$ $[0001]$. Hysteretic behaviour and the sharp switching appears at temperatures below 100 K. **c**, Temperature dependence of the anomalous Hall resistivity (ρ_H^A). A peak appears around 150 K. Since ρ_H^A was derived by extrapolating the high-field part of ρ_H to zero field, non-zero values can be observed just above T_C due to the short-range magnetic exchange interactions enhanced by high fields. **d**, σ dependence of σ_H^A . The σ -independent σ_H^A (i.e., $\sigma_H^A \sim (\sigma)^0 = \text{constant}$), below 100 K, puts this material into the intrinsic regime according to the unified model of AHE physics (for more details see [Supplementary Information](#))^{30,31}.

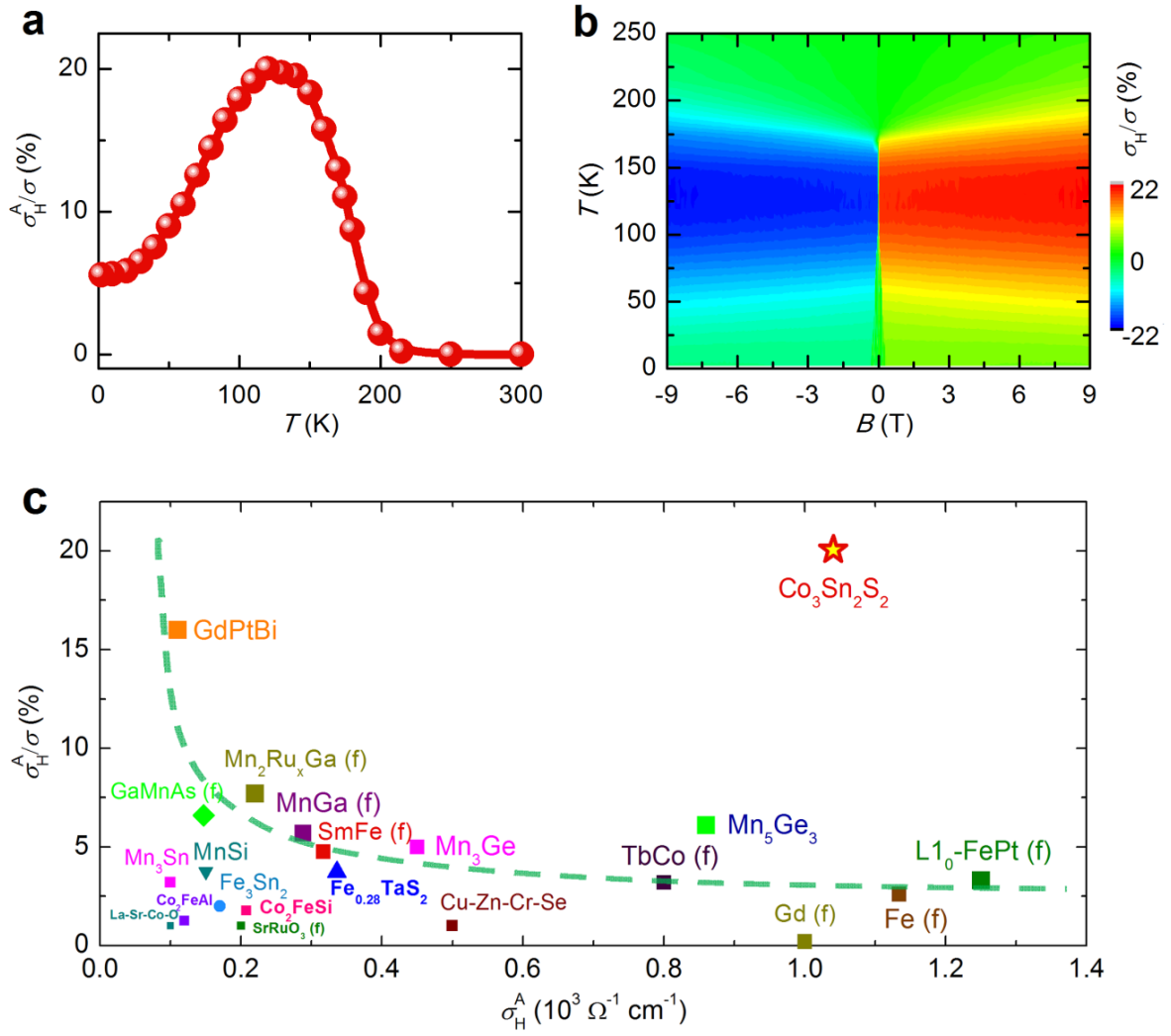


Figure 4 | Transport measurements of the AHA. **a**, Temperature dependence of the anomalous Hall angle (σ_H^A/σ) at zero magnetic field. Since the ordinary Hall effect vanishes at zero field, only the anomalous contribution prevails (see [Supplementary Information](#)). **b**, Contour plots of the Hall angle in the B - T space. **c**, Comparison of our σ_H^A -dependent AHA results and previously reported data for other AHE materials. "(f)" denotes thin-film materials. The dashed line is a guide to the eye. The reported data were taken from references that can be found in the [Supplementary Information](#).

Supplementary Information

Giant anomalous Hall angle in a half-metallic magnetic Weyl semimetal

Enke Liu^{1,2*}, Yan Sun^{1*}, Lukas M üchler³, Aili Sun¹, Lin Jiao¹, Johannes Kroder¹, Vicky S üß¹,
Horst Borrmann¹, Wenhong Wang², Walter Schnelle¹, Steffen Wirth¹, Sebastian T. B.
Goennenwein⁴, and Claudia Felser¹

¹ *Max-Planck Institute for Chemical Physics of Solids, 01187 Dresden, Germany*

² *Institute of Physics, Chinese Academy of Sciences, Beijing 100190, China*

³ *Department of Chemistry, Princeton University, Princeton, New Jersey 08544, USA*

⁴ *Institut für Festkörper- und Materialphysik, Technische Universität Dresden, 01062 Dresden, Germany*

(Dated: 22 November 2017)

1. Single crystals

The single crystals of $\text{Co}_3\text{Sn}_2\text{S}_2$ can be grown by several methods.



Fig. S1. Optical image of our single crystals.

* Enke.Liu@cpfs.mpg.de (E. L.)

* Yan.Sun@cpfs.mpg.de (Y. S.)

2. Structural characterizations

The crystals were characterized by powder X-ray diffraction as single phase with a Shandite-type structure. The lattice parameters at room temperature are $a = 5.3689 \text{ \AA}$ and $c = 13.176 \text{ \AA}$. Single crystals and orientations were assigned by single-crystal X-ray diffraction technique. However, an unambiguous assignment of the threefold axis is virtually impossible based on diffraction data only. This is due to a very particular situation as the unit cell is virtually cubic but also the arrangement of atoms in the structure show very little or no deviation, respectively, from cubic symmetry. Accordingly deviations in intensities of Bragg peaks are reflected in a small subset and quite hard to identify (Fig. S2).

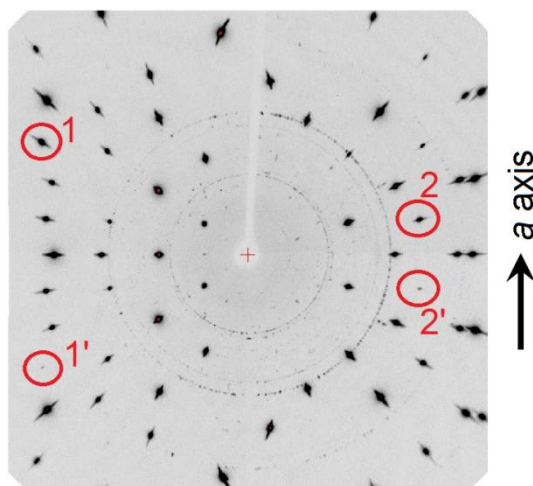


Fig. S2. Single-crystal XRD pattern observed at room temperature. Oscillation image taken while rocking the crystal by 32° about the a -axis of the FCC type cell. Spots violating horizontal mirror symmetry are highlighted and indicate the violation of cubic symmetry of the structure.

Supplementary Table S1. Crystal data and structure refinement for Co₃S₂Sn₂ at room temperature.

Empirical formula	Co ₃ S ₂ Sn ₂
Temperature	295(2) K
Wavelength	0.71073 Å
Crystal system	Trigonal
Space group	<i>R</i> -3 <i>m</i> : H
Unit cell dimensions	<i>a</i> = 5.3689(5) Å <i>c</i> = 13.176(2) Å (<i>a</i> = 5.3757(6) Å, α = 59.916(8) ° for primitive cell)
Volume	328.92(8) Å ³
<i>Z</i>	3
Density (calculated)	7.244 g/cm ³
Absorption coefficient	23.089 mm ⁻¹
F(000)	639
Crystal size	0.074 × 0.076 × 0.135 mm ³
Theta range for data collection	4.65 to 34.7 °
Index ranges	-4 ≤ <i>h</i> ≤ 8, -7 ≤ <i>k</i> ≤ 8, -17 ≤ <i>l</i> ≤ 21
Reflections collected	868
Independent reflections	195 [<i>R</i> (int) = 0.0223]
Refinement method	Full-matrix least-squares on F ²
Data / restraints / parameters	195 / 0 / 13
Goodness-of-fit on F ²	1.282
Final <i>R</i> indices [<i>I</i> > 2σ(<i>I</i>)]	<i>R</i> 1 = 0.0224, <i>wR</i> 2 = 0.0546
<i>R</i> indices (all data)	<i>R</i> 1 = 0.0226, <i>wR</i> 2 = 0.0547
Extinction coefficient	0.061(3)

3. Magnetic measurements

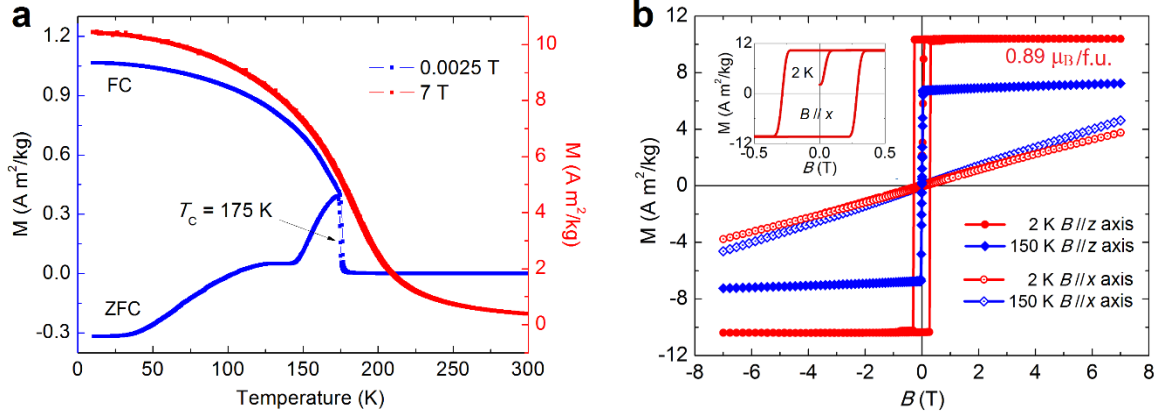


Fig. S3. (a) ZFC/FC measurements on temperature dependence of magnetization. The Curie temperature is located at $T_C = 175$ K. Around 140 K, there is an anomalous magnetic transition at low field of 0.0025 T (25 Oe) in the ZFC curve. However, this transition has been suppressed during the FC measurement. In higher fields, this weak transition also disappears, which deserves further study. (b) Field dependence of magnetization at 2 and 150 K with field along x (a) and z (c) axes. Inset shows the magnetization loop with hysteresis at 2 K with field along c axis. The field dependence of magnetization indicates there is a strong magneto-crystalline anisotropy in this compound with the moment along c axis. Along c axis, the magnetization rapidly saturates at a low field of 0.1 T. In a - b plane, the magnetization does not show any sign of saturation in magnetic fields up to 7 T. At 2 K, a saturated moment of $0.89 \mu_B/\text{f.u.}$ ($0.30 \mu_B/\text{Co}$) was observed in easy axis.

4. Theoretical calculations

The electronic calculations were carried out based on the density functional theory using the Vienna *ab-initio* simulation package (VASP)¹. The exchange and correlation energies were treated under the gradient approximation (GGA), following the Perdew–Burke–Ernzerhof parametrization scheme². The calculations were performed using the experimentally measured lattice parameters in this study ($a = 5.3689 \text{ \AA}$ and $c = 13.176 \text{ \AA}$).

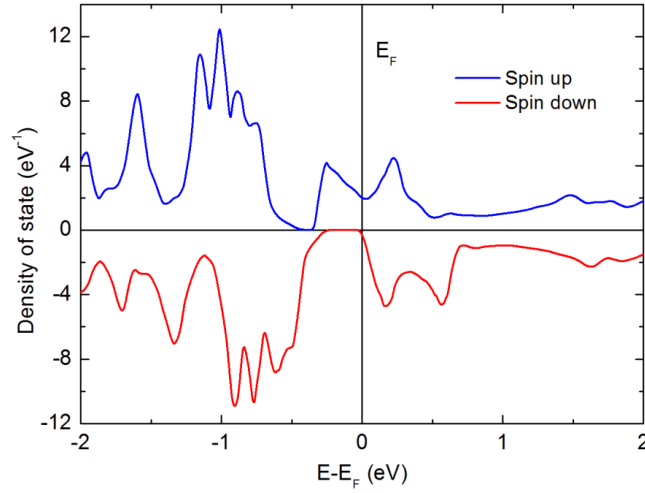


Fig. S4. Density of state (DOS) of Co₃Sn₂S₂ at ground state. For spin-up channel, the Fermi level is located in a pseudo-valley of DOS, indicating a (semi-)metal character. For spin-down channel, an energy gap with a width of about 0.30 eV appears. Nevertheless, the Fermi level is located very close to the conduction band. In total, a half-metal character can be expected in this compound.

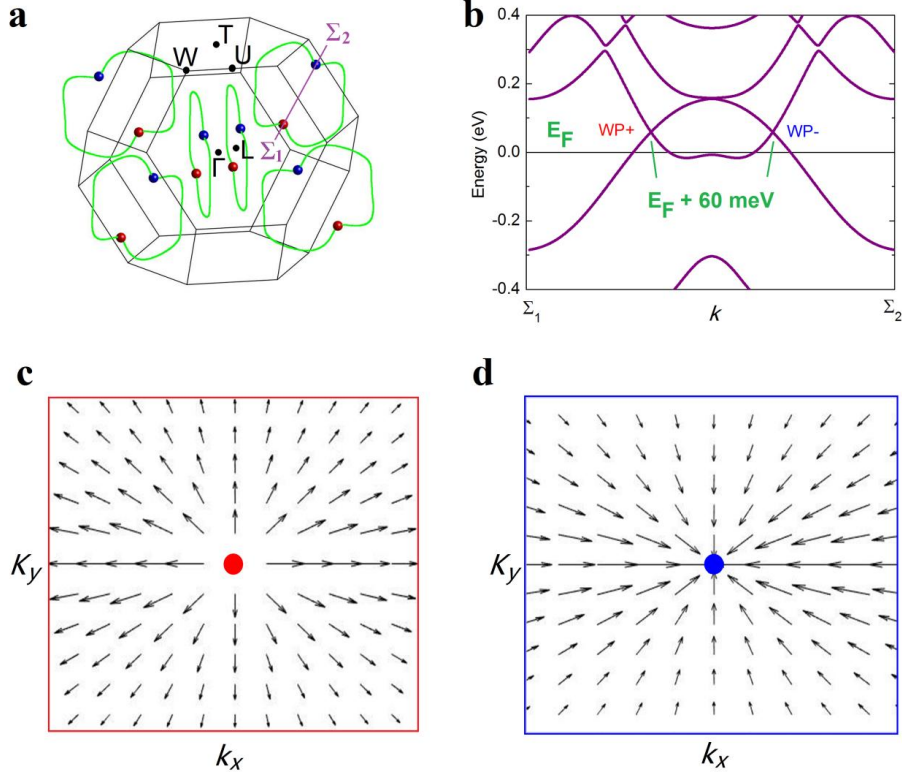


Fig. S5. **a**, Distribution of nodal lines in the BZ. A cut from Σ_1 to Σ_2 is shown. **b**, band structure along Σ_1 - Σ_2 path. Under SOC, a pair of linear crossings of Weyl points (WP+ and WP-) is presented at 60 meV above the Fermi level. The positions of WP+ and WP- of the momenta (k_x , k_y , k_z) are $2\pi (0.461/a, 0, 0.140/c)$ and $2\pi (0.693/a, 0, 0.960/c)$, respectively. **c** and **d**, sink and source of the monopoles of the Berry curvature at WP+ and WP- points, respectively. The topological charge is +1 and -1, respectively.

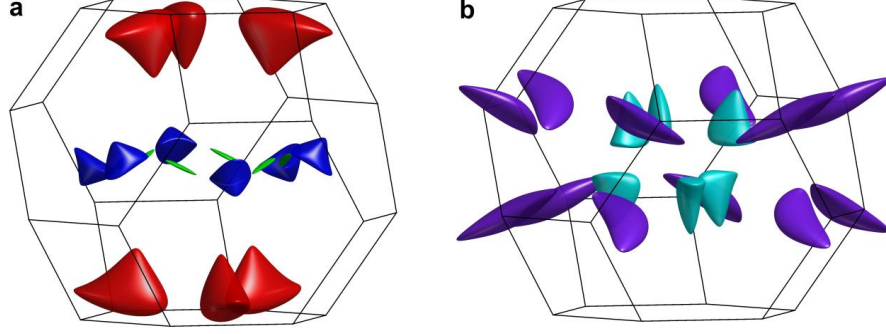


Fig. S6. Fermi surfaces of two bands crossing the Fermi level. Different colors indicate different parts of Fermi surface along different paths for every band. The calculations were performed with SOC. Only two bands cross the Fermi level. **a**, Fermi surface of band 43. **b**, Fermi surface of band 44. It can be seen the Fermi surfaces are not large, which is coherent with the low carrier density measured by transport experiments.

5. Transport measurements

The measurements were performed in an out-of-plane configuration of $I \parallel x$ [$2\bar{1}\bar{1}0$] and $B \parallel z$ [0001]. The temperature dependence of longitudinal charge resistivity (ρ) was measured in fields of 0 and 9 T, as shown in Fig. S7(a). The corresponding longitudinal charge conductivity was calculated by $\sigma = 1/\rho$, as shown in Fig. S7(b). The original data of Hall transport were extracted by antisymmetric processing in order to eliminate the magnetoresistance (MR) signals due to the misalignment of the voltage leads. For longitudinal charge resistivity, the ρ - B is odd and ρ_H - B is even, and we can extract the pure Hall component using $\rho_H = 1/2[\rho_H(B) - \rho_H(-B)]$, while the pure charge resistivity component using $\rho = 1/2[\rho(B) + \rho(-B)]$. The extracted results are shown in Fig. S8. The saturation and coercive fields of the loop behaviour for magnetization and Hall resistivity were determined by magnetic and transport measurements, as shown in Fig. S9. The pure anomalous Hall resistivity (ρ_H^A) was derived by extrapolating the high-field part of ρ_H back to zero field, as shown in Fig. S10. The anomalous Hall conductivity was calculated by $\sigma_H^A = -\rho_H^A / ((\rho_H^A)^2 + \rho^2)$. Here ρ_H^A is the anomalous Hall resistivity at zero field; ρ is the longitudinal charge resistivity at zero field. The σ dependence of σ_H^A of our material has been discussed in the framework of unified theory, as shown in Fig. S11.

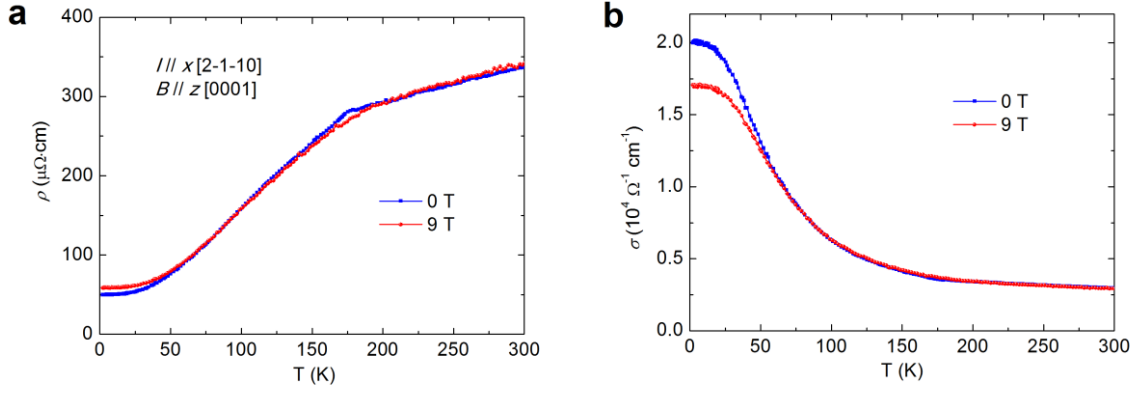


Fig. S7. Temperature dependence of longitudinal charge resistivity (ρ) (a) and longitudinal charge conductivity (σ) (b) in fields of 0 and 9 T. Due to the spin-dependent scattering below T_C , a rapid drop in ρ produces a relatively large RRR ($\rho_{300\text{K}}/\rho_{2\text{K}}$) of 6.7. This value of RRR also confirms the extraordinary quality of our crystals. At the same time, the charge conductivity is not very high, and rapidly decreases from $\sim 2 \times 10^4 \Omega^{-1} \text{cm}^{-1}$ at 2 K to $\sim 0.5 \times 10^4 \Omega^{-1} \text{cm}^{-1}$ around T_C . For more detailed information, please see Table S2.

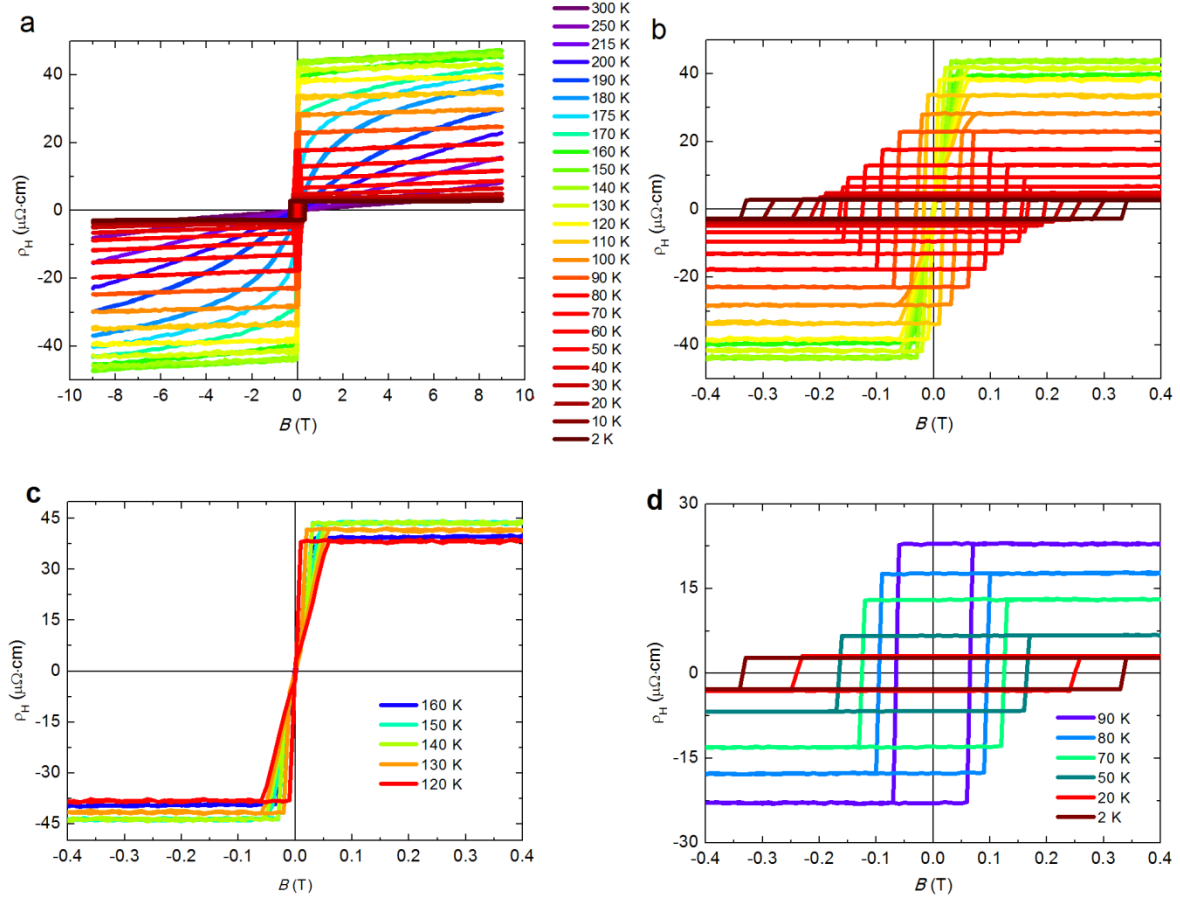


Fig. S8. Field dependence of Hall resistivity (ρ_H). (a) All data measured in -9 ~ 9 T from 300 to 2 K. (b) Data measured in -0.4 ~ 0.4 T from 300 to 2 K. (c) Data measured in -0.4 ~ 0.4 T from 160 to 120 K. (d) Data measured in -0.4 ~ 0.4 T from 100 to 2 K. A maximum of Hall resistivity appears around 150 K. A hysteresis appears below 150 K and a coercive field can be observed below 120 K. The coercive field decreases with decreasing temperature, as shown in Fig. S9. Below 100 K, a sharp switch with a rectangle shape in Hall resistivity loop can be seen owing to the switching of magnetization and Berry curvature.

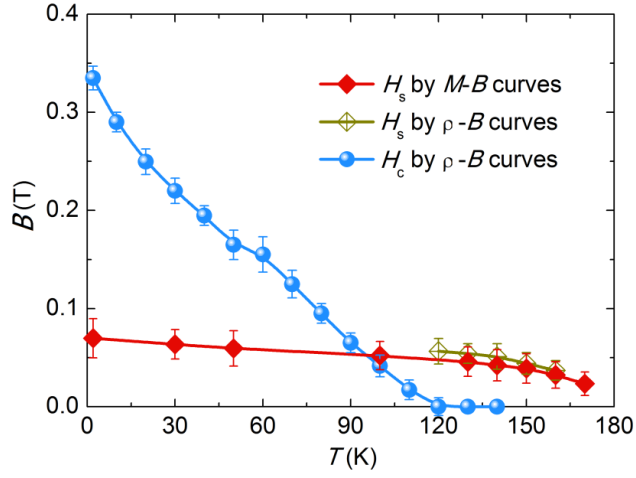


Fig. S9. Saturation and coercive fields of the loop behaviour for magnetization and Hall resistivity determined by magnetic and transport measurements, taken from Fig. S8.

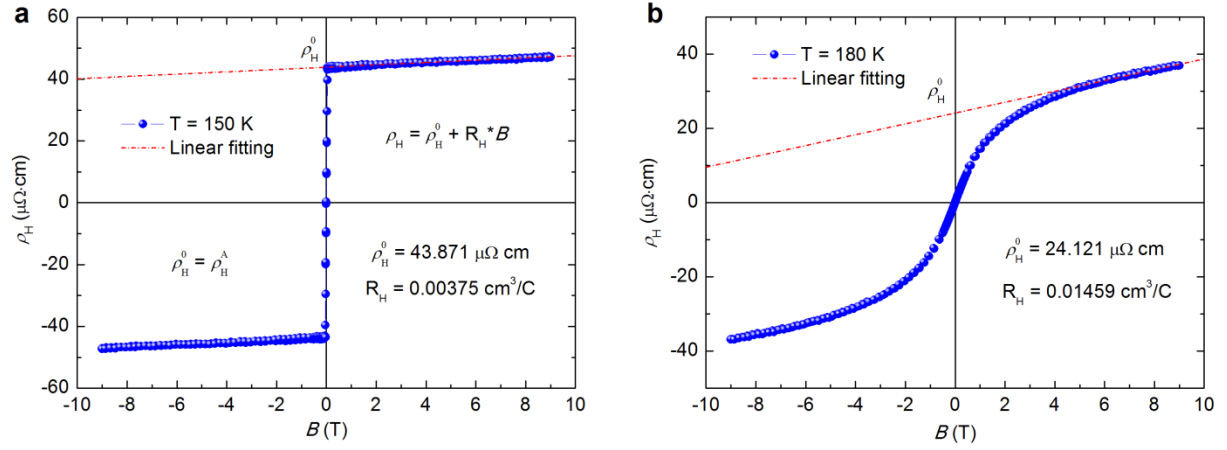


Fig. S10. Deriving the pure anomalous Hall resistivity ($\rho_H^A = \rho_H^0$) by extrapolating the high-field part of ρ_H back to zero field. (a) $T = 150$ K, below T_C . (b) $T = 180$ K, slightly above T_C . The ordinary Hall contribution vanishes at zero field, only the anomalous contribution prevails. Only demonstrations at two temperatures were shown here.

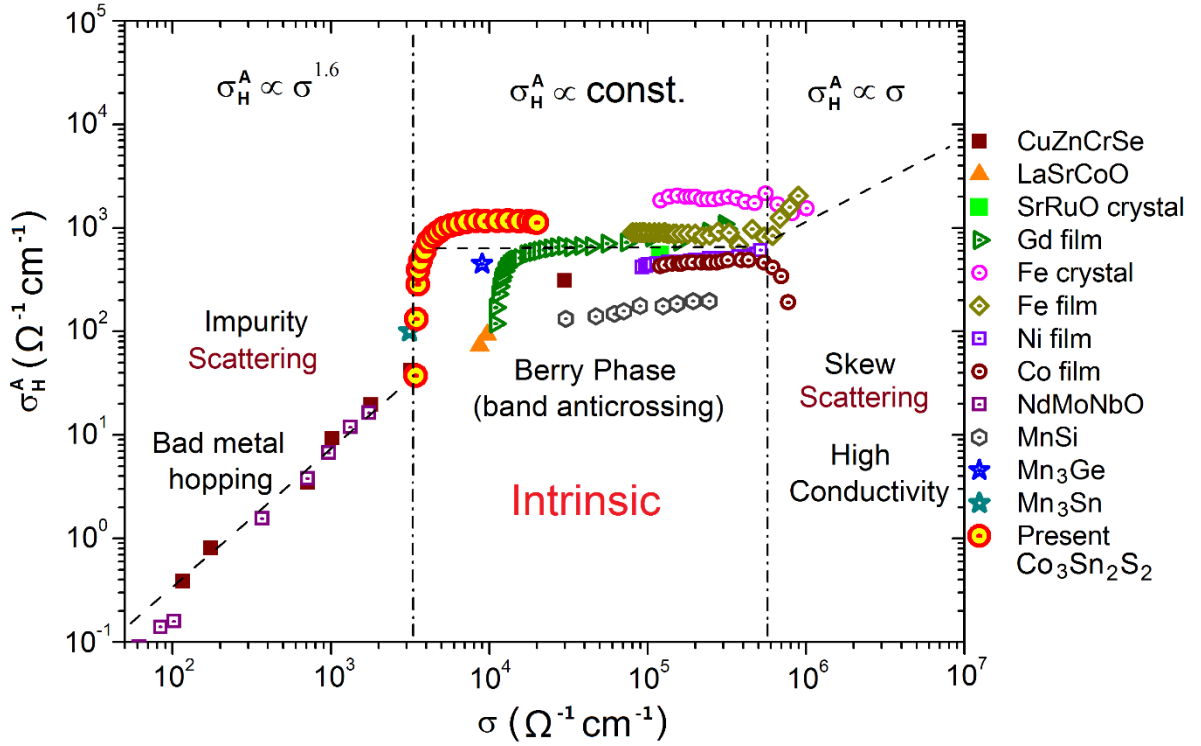


Fig. S11. σ dependence of σ_H^A in the framework of unified theory^{3,4}. Here we use the absolute amplitudes of σ_H^A without the negative sign. The data of other materials were taken from references and therein^{5,6}. Our present result shows a σ -independent σ_H^A below 100 K, i.e., $\sigma_H^A \sim (\sigma)^0 = \text{constant}$. Our data matches the predictions of the model in which three regimes of the AHA is identified. Co₃Sn₂S₂ is located into the intrinsic regime dominated by the Berry-phase curvature, not by the extrinsic scattering events. Here the Berry-phase curvature just comes from the Weyl nodes and nodal lines with band anticrossing in Co₃Sn₂S₂.

Table S2. Longitudinal charge resistivity (ρ), longitudinal charge conductivity (σ), anomalous Hall effect (ρ^A_H), ordinary Hall coefficient (R_H), carrier concentration (n) and carrier mobility (μ) at different temperatures. The ordinary Hall coefficient (R_H) was extracted by linearly fitting the high-field part of ρ_H - B , as shown in Fig. S10. The carrier concentration (n) was calculated by $n = 1/R_H e$ (e is the basic electric charge). The carrier mobility (μ) was calculated by $\mu = R_H/\rho$ (ρ is the longitudinal charge resistivity at zero field). One can see a low carrier density ($\sim 10^{21} \text{ cm}^{-3}$) in the whole temperature range.

T	ρ (ρ_{xx})	σ (σ_{xx})	ρ^A_H	R_H	n	μ
K	$\mu\Omega \text{ cm}$	$10^4 \Omega^{-1} \text{ cm}^{-1}$	$\mu\Omega \text{ cm}$	cm^3/C	10^{21} cm^{-3}	$\text{cm}^2 \text{ V}^{-1} \text{ s}^{-1}$
300	342.85	0.29167	0	0.00511	1.22211	14.91649
250	319.43424	0.31305	0	0.00910	0.686884	28.48494
215	301.56739	0.3316	0.96123	0.01632	0.382917	54.12414
200	289.97313	0.34486	5.178	0.02000	0.312444	68.98423
190	289.15785	0.34583	12.521	0.01948	0.320916	67.35256
180	287.1237	0.34828	24.121	0.01459	0.428452	50.80528
175	278.07874	0.35961	30.138	0.01154	0.541536	41.50355
170	269.47913	0.37109	34.64	0.00918	0.680512	34.08155
160	263.1976	0.37994	41.449	0.00460	1.35914	17.4717
150	244.18173	0.40953	43.871	0.00375	1.66682	15.35603
140	229.68321	0.43538	43.722	0.00254	2.45685	11.07574
130	214.53963	0.46611	41.39	0.00195	3.19742	9.11116
120	197.62724	0.506	38.519	0.000914	6.83562	4.62653
110	175.36763	0.57023	33.619	0.00144	4.35461	8.18429
100	157.92541	0.63321	28.223	0.00183	3.40965	11.60696
90	139.70885	0.71577	22.922	0.00199	3.13512	14.26926
80	121.91201	0.82026	17.696	0.00228	2.73853	18.72043
70	106.32703	0.94049	12.991	0.00252	2.47991	23.70282
60	90.32007	1.10717	9.354	0.00271	2.30915	29.96697
50	76.05311	1.31487	6.678	0.00231	2.70019	30.43463
40	65.02781	1.5378	4.805	0.00215	2.91282	32.9964
30	56.50824	1.76965	3.657	0.00189	3.30983	33.41664
20	52.04148	1.92154	3.048	0.00125	4.99815	24.0282
10	50.22827	1.99091	2.821	0.000948	6.59129	18.87824
2	49.95624	2.00175	2.776	0.000797	7.84127	15.95527

Table S3. Summary of longitudinal charge conductivity (σ), anomalous Hall conductivity (σ_H^A), and anomalous Hall angle (AHA) of currently studied magnetic materials. Some AHA values are calculated by using the data from the references. Here we use the absolute amplitudes of σ_H^A without the negative sign. Only the maximum values of AHA are adopted here.

System	σ	σ_H^A	AHA= σ_H^A/σ	Refs.
	$10^4 \Omega^{-1} \text{cm}^{-1}$	$\Omega^{-1} \text{cm}^{-1}$	%	
Mn ₃ Ge	0.9000	450	5	7
Mn ₃ Sn	0.3125	100	3.2	8
GdPtBi	0.0690	110	16	9
MnGa film	0.5052	288	5.7	10
L1 ₀ -FePt film	3.7880	1250	3.3	11
TbCo film	2.5000	800	3.2	12
Mn ₂ Ru _x Ga	0.2860	220	7.7	13
SmFe film	0.6640	317	4.75	14
Fe _{0.28} TaS ₂	0.9009	336	3.73	15
GaMnAs film	0.2222	147	6.6	16
SrRuO ₃ film	2.0000	200	1	17
Co ₂ FeSi	1.1750	208	1.77	18
Co ₂ FeAl	0.9600	120	1.25	18
Fe film	4.3620	1134	2.6	4
Gd film	50.0000	1000	0.2	4
La-Sr-Co-O	1.0000	100	1	4
Cu-Zn-Cr-Se	5.0000	500	1	4
MnSi	0.4000	150	3.75	19
Mn ₅ Ge ₃	1.4100	860	6.1	20
Co₃Sn₂S₂	0.5650	1130	20	Present work

Supplementary References

1. Kresse, G. and Furthmüller, J. Efficient iterative schemes for *ab initio* total-energy calculations using a plane-wave basis set. *Phys. Rev. B* **54**, 11169-11186 (1996).
2. Perdew, J. P., Burke, K. and Ernzerhof, M. Generalized gradient approximation made simple. *Phys. Rev. Lett.* **77**, 3865-3868 (1996).
3. Onoda, S., Sugimoto, N. and Nagaosa, N. Intrinsic versus extrinsic anomalous Hall effect in ferromagnets. *Phys. Rev. Lett.* **97**, 126602 (2006).
4. Miyasato, T. *et al.* Crossover behavior of the anomalous Hall effect and anomalous Nernst effect in itinerant ferromagnets. *Phys. Rev. Lett.* **99**, 086602 (2007).
5. Onoda, S., Sugimoto, N. and Nagaosa, N. Quantum transport theory of anomalous electric, thermoelectric, and thermal Hall effects in ferromagnets. *Phys. Rev. B* **77**, 165103 (2008).
6. Asamitsu, A. *et al.* Anomalous Hall effect and Nernst effect in itinerant ferromagnets. *J. Magn. Mater.* **310**, 2000-2002 (2007).
7. Nayak, A. K. *et al.* Large anomalous Hall effect driven by a nonvanishing Berry curvature in the noncollinear antiferromagnet Mn₃Ge. *Sci. Adv.* **2**, e1501870 (2016).
8. Nakatsuji, S., Kiyohara, N. and Higo, T. Large anomalous Hall effect in a non-collinear antiferromagnet at room temperature. *Nature* **527**, 212 (2015).
9. Suzuki, T. *et al.* Large anomalous Hall effect in a half-Heusler antiferromagnet. *Nat. Phys.* **12**, 1119-1123 (2016).
10. Wu, F. *et al.* Electrical transport properties of perpendicular magnetized Mn-Ga epitaxial films. *Appl. Phys. Lett.* **96**, 042505 (2010).
11. Yu, J. *et al.* Magnetotransport and magnetic properties of molecular-beam epitaxy L1₀ FePt thin films. *J. Appl. Phys.* **87**, 6854-6856 (2000).
12. Kim, T. W. and Gambino, R. J. Composition dependence of the Hall effect in amorphous Tb_xCo_{1-x} thin films. *J. Appl. Phys.* **87**, 1869-1873 (2000).
13. Thiagarajah, N. *et al.* Giant spontaneous Hall effect in zero-moment Mn₂Ru_xGa. *Appl. Phys. Lett.* **106**, 122402 (2015).
14. Kim, T. W., Lim, S. H. and Gambino, R. J. Spontaneous Hall effect in amorphous Tb-Fe and Sm-Fe thin films. *J. Appl. Phys.* **89**, 7212-7214 (2001).
15. Dijkstra, J., Zijlema, P. J., Bruggen, C. F. v., Haas, C. and Groot, R. A. d. Band-structure calculations of Fe_{1/3}TaS₂ and Mn_{1/3}TaS₂, and transport and magnetic properties of Fe_{0.28}TaS₂. *J. Phys.: Condens. Matter* **1**, 6363 (1989).
16. Pu, Y., Chiba, D., Matsukura, F., Ohno, H. and Shi, J. Mott relation for anomalous Hall and Nernst effects in Ga_{1-x}Mn_xAs ferromagnetic semiconductors. *Phys. Rev. Lett.* **101**, 117208 (2008).
17. Fang, Z. *et al.* The anomalous Hall effect and magnetic monopoles in momentum space. *Science* **302**, 92-95 (2003).
18. Imort, I. M., Thomas, P., Reiss, G. and Thomas, A. Anomalous Hall effect in the Co-based Heusler compounds Co₂FeSi and Co₂FeAl. *J. Appl. Phys.* **111**, 07D313 (2012).

19. Manyala, N. *et al.* Large anomalous Hall effect in a silicon-based magnetic semiconductor. *Nat. Mater.* **3**, 255 (2004).
20. Zeng, C., Yao, Y., Niu, Q. and Weitering, H. H. Linear magnetization dependence of the intrinsic anomalous Hall effect. *Phys. Rev. Lett.* **96**, 037204 (2006).